ORIGINAL PAPER

A Discrete Element Model for Predicting Shear Strength and Degradation of Rock Joint by Using Compressive and Tensile Test Data

T. Kazerani · Z. Y. Yang · J. Zhao

Abstract A discrete element model is proposed to examine rock strength and failure. The model is implemented by UDEC, which is developed for this purpose. The material is represented as a collection of irregular-sized deformable particles interacting at their cohesive boundaries. The interface between two adjacent particles is viewed as a flexible contact whose constitutive law controls the material fracture and fragmentation properties. To reproduce rock anisotropy, an orthotropic cohesive law is developed for the contacts, which allows their shear and tensile behaviors to be different from each other. Using a combination of original closed-form expressions and statistical calibrations, a unique set of the contact microparameters are found based on the uniaxial/triaxial compression and Brazilian tension test data of a plaster. Applying the obtained microparameters, joint specimens, made of the same plaster, are simulated, where the comparison of the obtained results to laboratory data shows a reasonable agreement.

Keywords Discrete element method · Orthotropic cohesive contact model · Microparameter · Rock joint · Degradation

T. Kazerani (✉) · J. Zhao
Ecole Polytechnique Fédérale de Lausanne (EPFL),
Laboratoire de Mécanique des Roches (LMR),
Station 18, 1015 Lausanne, Switzerland
e-mail: tohid.kazerani@epfl.ch

Z. Y. Yang
Department of Civil Engineering, Tamkang University,
Taipei, Taiwan

1 Introduction

The Discrete Element Method (DEM) has been vastly used to capture the sequences of separation and reattachment observed in the fragmentation process of brittle materials. Formulation and development of the DEM have progressed over a long time since the pioneering study of Cundall (1971). Recently, Jing and Stephansson (2007) have comprehensively provided the fundamentals of the DEM and its application in rock mechanics.

According to the solution algorithm used, the DEM implementations can be divided into two groups of explicit and implicit formulations. The most popular representations of the explicit DEM are the computer codes of PFC (ITASCA Consulting Group, Inc. 2008a) and UDEC (ITASCA Consulting Group, Inc. 2008b).

One use of the explicit DEM is to model brittle material as a dense packing of irregular-sized particles interacting at their boundaries. The significant advantage of this type of simulation, which has been predominantly implemented by PFC, is to model the crack as a real discontinuity (Yoon 2007; Potyondy and Cundall 2004; Cho et al. 2007; Diederich 2000). However, any DEM simulation crucially needs calibration. Yoon (2007) showed that the PFC microparameters can be calibrated to fit concurrently the Young's modulus, Poisson's ratio, and uniaxial compressive strength of rock. However, the predicted Brazilian tensile strength has been approximately 0.25 of the uniaxial compressive strength (Yoon 2007; Potyondy and Cundall 2004; Cho et al. 2007; Diederich 2000). Comparing various types of rock, this value is unrealistically high, where the ratio of the tensile to the compressive strength is typically reported around 0.05–0.1 (Hoek and Brown 1998). Moreover, Potyondy and Cundall (2004) reported that calibrating PFC to the uniaxial strength gives a very low triaxial strength.

Different solutions have been proposed to improve the PFC results, e.g., the so-called *cluster* (Potyondy and Cundall 2004) or *clump* logic (Cho et al. 2007). However, in addition to execution difficulties, these logics are suffering from some disadvantages. For example, since each cluster or clump is composed of several particles, its size is perforce much larger than that of rock mineral. Moreover, some PFC microparameters, e.g., coefficient of friction, contact modulus, and parallel bond modulus, show no effect on the model response and consequently are deprived of any physical sense (Yoon 2007; Potyondy and Cundall 2004; Cho et al. 2007).

Some other DEM developments have been individually provided, e.g., Wang and Tonon (2009) created a 3D DEM code, based on the spherical particles, which was used to reproduce the experimental triaxial test data of Lac du Bonnet granite. Using a similar model in which rock was represented by bonded spherical particles; Schöpfer et al. (2009) investigated the dependence of elasticity, strength and friction angle on rock porosity and crack density. Lobo-Guerrero et al. (2006) developed a DEM simulation to examine the effects of grain breakage in granular materials subjected to uniaxial compression. Lobo-Guerrero and Vallejo (2010) applied this model on fiber-reinforced granular materials and reached promising results. Mahabadi et al. (2010) used a coupled finite–discrete element code to examine rock heterogeneity and rock avalanche as well as the Brazilian test on homogeneous and layered rock.

The validity of these DEM models is restricted, as they only predict a limited number of rock experimental behaviors. Hence, the necessity of developing a comprehensive model to involve a vast variety of rock physical characteristics is deeply felt. The novelty of this research is to develop a DEM model, which can concurrently predict the compressive, tensile, and shear behaviors of rock. Since finding the DEM microparameters is still an open question, our objective also includes establishing a definite framework for model calibration. Note that reproducing the experimental data is not our major intention. In fact, we aim at offer a physical interpretation for each DEM microparameter in terms of the standard laboratory properties. These interpretations help understand how rock micromechanical properties controls its macroscopic response.

The model presented in this study was initially introduced by the authors, where they successfully simulated compressive and tensile behavior of hard and soft rocks by employing polygonal rigid particles (Kazerani 2010). We developed the model by adopting deformable particles and an orthotropic cohesive behavior for contacts constitutive law.

Laboratory tests on plaster samples are simulated to verify the model validity. First, the standard experiments,

i.e., the uniaxial/triaxial compression and the Brazilian tension, are modeled. The obtained results are shown to lead a unique set of the model microparameters that fit the material macroscopic responses in terms of the Brazilian tensile strength, compressive strength, internal friction angel, internal cohesion, Young's modules, and Poisson's ratio. Using the obtained microparameters, plaster joint specimens are ultimately simulated and the results will be compared with those of laboratory.

2 UDEC Numerical Modeling

As a finite deference–discrete element coupled code, UDEC permits two-dimensional plane-strain and plane-stress analyses. As mentioned, rock material is to be modeled as assemblage of distinct elastic particles interacting at their contacts (Fig. 1), where each particle is composed of the Constant-Strain Triangular (CST) elements.

A perturbation within this particle assemblage, caused by an applied excitation, propagates through the whole system and leads to the particles movement. The solution scheme is identical to that used by the explicit finite difference method for continuum analysis. Solving procedure in UDEC alternates between the application of a stress-displacement law at all the contacts, and the Newton's second law for all the particles. The contact stress-displacement law is used to find the contact stresses from the known displacements. The Newton's second law gives the particle motion resulting from the known forces acting on them. The motion is calculated at the grid points of the CST elements within each elastic particle. Then, application of the material constitutive relations gives new stresses within the elements. Figure 2 schematically presents the calculation cycle in UDEC together with a brief review of basic equations.

2.1 Orthotropic Cohesive Contact Model

The model failure behavior is controlled by the contact constitutive law. Hence, failure characteristics of rock must
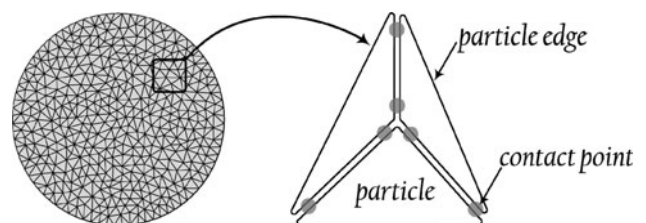

Fig. 1 A representative particle assemblage used for the Brazilian test simulation, and configuration of model-constructing particles and contacts
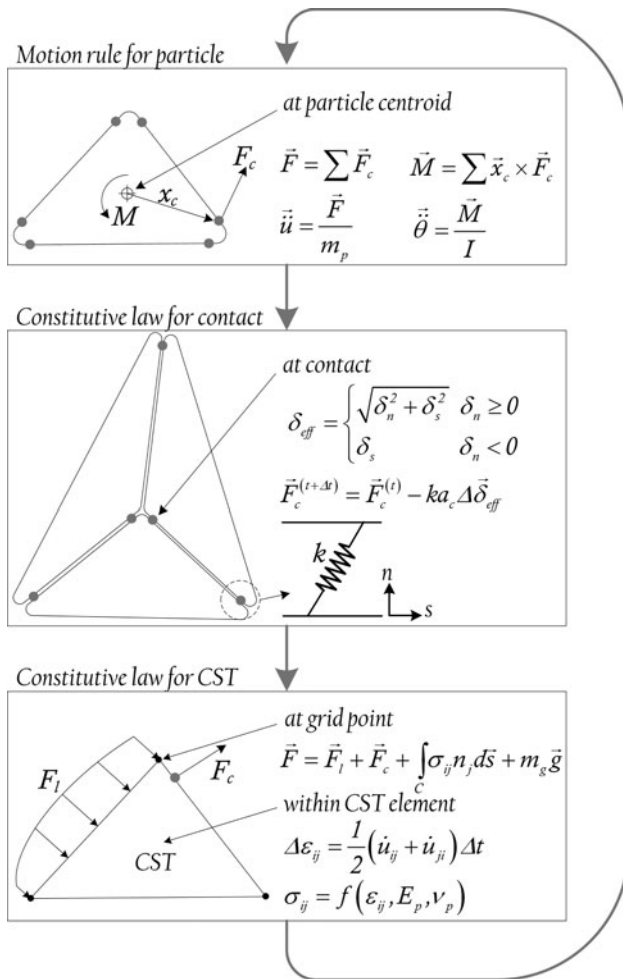
Fig. 2 Calculation cycle in UDEC (ITASCA Consulting Group, Inc. 2008a)

be appropriately reflected in the contact law. A cohesive contact model is developed for this purpose. It acts like some glue cohering particles together, which also follows an orthotropic behavior. It is assumed to have a decaying stiffness in the pre-failure stage in order to represent the damage behavior of the fracture process zone.

Depending on whether a contact undergoes tension or shear, it endures either gradual or perfect stress softening after its strength is exceeded. In tension, the supposed glue gradually loses its stress and is stretched up to a length called *contact cohesive displacement*, beyond which the contact will no longer endure stress. In shear, the contact stress abruptly decreases to a residual frictional strength, which represents the friction acting on the fractured surface.

The stress σ applied on the contact surface is defined as

$$\sigma = \sigma(\delta_{\text{eff}}, k_{\text{t}}, k_{\text{s}}, t_{\text{c}}, c_{\text{c}}, \phi_{\text{c}}, D) \qquad (1)$$

where δ_{eff} is the contact effective displacement, and k_{t} and k_{s} denote the contact initial stiffness coefficients in tension and shear, respectively. The parameters t_{c}, c_{c}, and ϕ_{c}

characterize the strength of contact. They, respectively, referred to as contact tensile strength, contact cohesion, and contact friction angle. D is the contact damage variable. In mixed-mode separation, i.e., concurrent existence of normal and shear displacements, δ_{eff} is defined as

$$\delta_{\text{eff}} = \begin{cases} \sqrt{\delta_{\text{n}}^2 + \delta_{\text{s}}^2} & \delta_{\text{n}} \geq 0 \\ \delta_{\text{s}} & \delta_{\text{n}} < 0 \end{cases} \qquad (2)$$

where δ_{n} and δ_{s} are the normal separation and shear sliding over the contact surface and δ_{n} is assumed positive where the contact undergoes opening (tension).

2.1.1 Tensile Behavior of Contact

Contact cohesive stress in tension is expressed as

$$\sigma = \begin{cases} k_{\text{t}}\delta_{\text{eff}} \exp(-\delta_{\text{eff}}/\delta_{\text{ct}}) & \delta_{\text{eff}} \leq \delta_{\text{ct}} \\ t_{\text{c}}(1-D) & \delta_{\text{eff}} = \delta_{\text{max}} \\ k_{\text{red}}\delta_{\text{eff}} & \delta_{\text{eff}} < \delta_{\text{max}} \end{cases} \begin{matrix} \\ \delta_{\text{ct}} < \delta_{\text{eff}} \leq \delta_{\text{ut}}. \end{matrix} \\ 0 \qquad \delta_{\text{eff}} > \delta_{\text{ut}} \qquad (3)$$

In hardening stage ($\delta_{\text{eff}} \leq \delta_{\text{ct}}$), the governing equation is the exponential traction–separation law described by Xu and Needleman (1996) (Fig. 3a). δ_{ct} is the critical tensile displacement of contact beyond which cohesive softening happens, and δ_{ut} is the ultimate tensile displacement of contact at which contact entirely loses its cohesive strength. In this stage, stress-displacement behavior is elastic, i.e., the unloading and reloading paths are the same and no energy dissipates in contact.

As illustrated in Fig. 3a, at the peak point $\sigma = t_{\text{c}}$ and $\delta_{\text{eff}} = \delta_{\text{ct}}$. Substituting these values in the first line of Eq. 3 and solving it for δ_{ct} yields

$$\delta_{\text{ct}} = e\frac{t_{\text{c}}}{k_{\text{t}}} \qquad (4)$$

where $e = \exp(1)$ is the base of the natural logarithm.

In softening stage ($\delta_{\text{ct}} < \delta_{\text{eff}} \leq \delta_{\text{ut}}$), contact is permitted to release energy during unloading–reloading cycles. δ_{max} is then defined as the maximum effective displacement that contact has ever undergone (Fig. 3a). δ_{max} is δ_{eff}, when contact is increasingly opened, and held fixed as it undergoes unloading and reloading until δ_{eff} again reaches δ_{max}.

The damage variable is defined as follows:

$$D = \frac{\delta_{\text{max}} - \delta_{\text{ct}}}{\delta_{\text{ut}} - \delta_{\text{ct}}}. \qquad (5)$$

As contact undergoes softening, D irreversibly increases from 0 to 1 or remains constant, even if multiple unloading–reloading cycles happen.

Fig. 3 Stress-displacement behavior of cohesive contact model (*arrows* denote loading, unloading and reloading paths)

a tensile behavior

b compressive–shear behavior
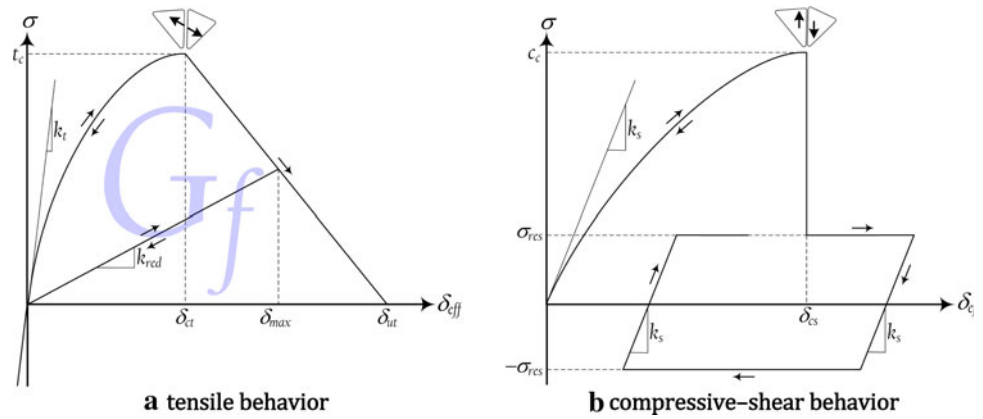
In unloading–reloading cycles ($\delta_{eff} < \delta_{max}$), contact follows a linear stress-displacement path, where k_{red} is defined as the secant stiffness at the point with an effective displacement equal to δ_{max} (see Fig. 3a).

2.1.2 Compressive-Shear Behavior of Contact

When contact is sheared under compression, the stress-displacement law is described as

$$\sigma = \begin{cases} k_s\delta_{eff}\exp(-\delta_{eff}/\delta_{cs}) & \delta_{eff} \leq \delta_{cs} \\ \sigma_{res} = -k_t\delta_n\tan(\phi_c) & \delta_{eff} > \delta_{cs} \end{cases}. \quad (6)$$

Similarly, the critical shear displacement of contact is calculated as follows:

$$\delta_{cs} = e\frac{c_c}{k_s}. \quad (7)$$

The unloading–reloading path of contact is linear as demonstrated in Fig. 3b, where the contact stress increment is calculated as

$$\Delta\sigma = \begin{cases} k_s\Delta\delta_{eff} & \sigma < \sigma_{res} \\ 0 & \sigma = \sigma_{res} \end{cases}. \quad (8)$$

Ultimately, the normal and shear components of contact force are obtained as

$$F_n = \begin{cases} -\sigma\frac{\delta_n}{\delta_{eff}}a_c & \delta_n \geq 0 \\ -k_t\delta_na_c & \delta_n < 0 \end{cases} \text{ and } F_s = -\sigma\frac{\delta_s}{\delta_{eff}}a_c \quad (9)$$

where a_c is the contact surface area.

2.1.3 Contact Fracture Energy

According to the Griffith–Irwin's fracture criterion, the condition necessary for fracture propagation is if sufficient energy is provided to detach material thereby increase the fractured surface. By definition, the Griffith's fracture energy, G_f is the rate of this energy per unit area along the fracture edge. The area under the curve in Fig. 3a represents the energy needed to fully open the unit area of

contact surface. Since contact is the numerical representation of fracture, the area under the curve should be equal to G_f:

$$G_f = \int_0^{\delta_{ut}} \sigma d\delta_{eff} = t_c\delta_{ct}(e-2) + t_c\frac{\delta_{ut}-\delta_{ct}}{2}. \quad (10)$$

2.1.4 Implementation of Developed Contact Model in UDEC

The source code of UDEC should be developed to implement the proposed contact model. The flowchart presented in Fig. 4 illustrates the algorithm used to carry out the formulation. It merely includes those equations that are related to the contact stress calculation.

2.2 Microparameters

The parameters involved in modeling are classified under the term *microparameter*. Table 1 lists them along with the analogous material properties.

Since the simulation is deeply affected by the microparameters, they must be appropriately set such that the model reproduces a response similar to that of physical material. To reach this purpose, the relation between the microparameters and the model behavior should be investigated. This is done by establishing analytical and statistical equations, which explicitly define and interpret each model macroscopic response in terms of the microparameters.

2.2.1 Physical Interpretation of Contact Stiffness Coefficient

In numerical simulation of structures involving bodies in contact, the effect of ill-conditioning may destabilize the solution. Briefly speaking, this problem is raised due to the lack of appropriate judgment about the contact stiffness. As commonly thought, the ideal choice for the contact

Fig. 4 Algorithm implemented in UDEC to calculate contact stress in terms of contact separation mode and effective displacement
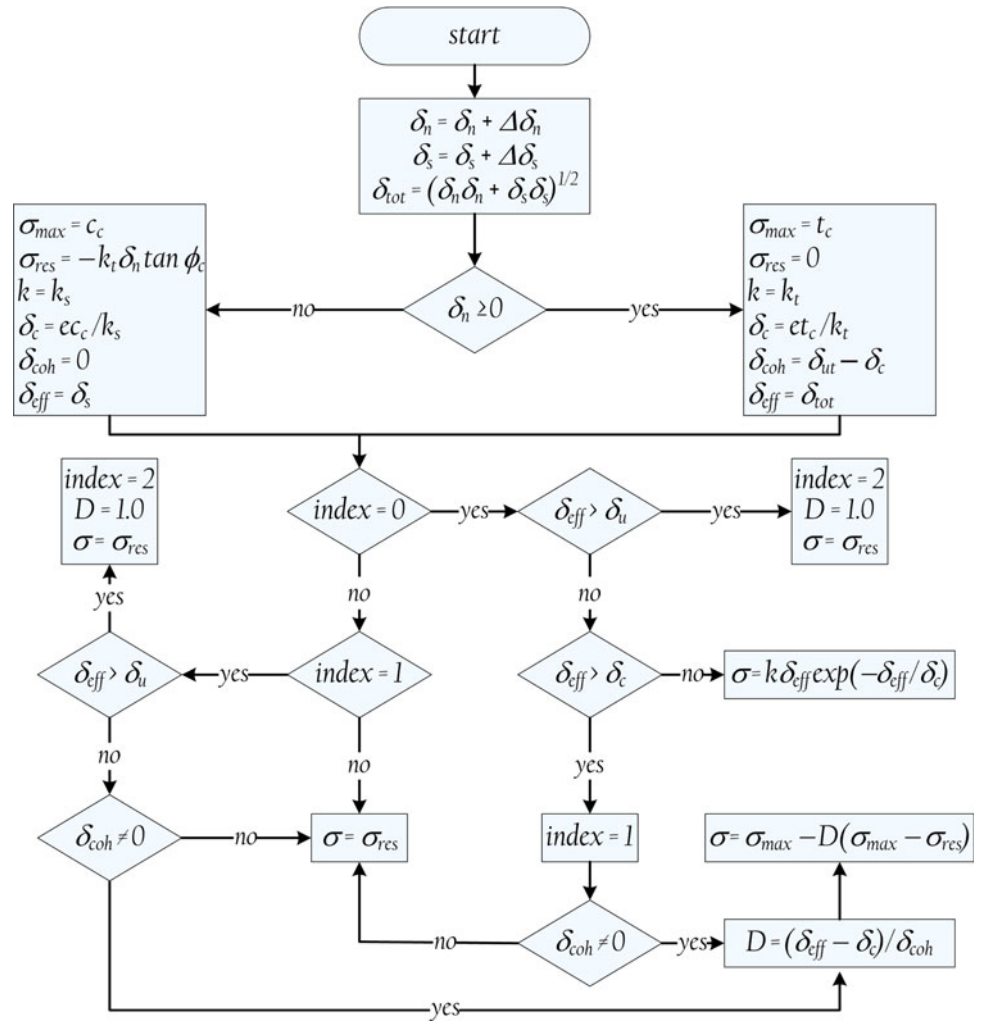

Table 1 Material properties and model microparameters

Material property	Model microparameter
Elasticity	*Particle*
Young's modulus (E)	Young's modulus (E_p)
Poisson's ratio (v)	Poisson's ratio (v_p)
Strength	*Contact*
Fracture toughness in mode-I (K_{IC})	Initial tensile stiffness coefficient (k_t)
Fracture toughness in mode-II (K_{IIC})	Initial shear stiffness coefficient (k_s)
Brazilian strength (σ_t)	Tensile strength (t_c)
Internal cohesion (C)	Cohesion (c_c)
Internal friction angle (ϕ)	Friction angle (ϕ_c)
Uniaxial compressive strength (σ_c)	Ultimate tensile displacement (δ_{ut})

stiffness is to take it as infinite to prevent any reduction in the global stiffness of the structure. However, this assumption causes numerical inconsistencies within the FEM solver or the DEM contact force algorithm (ITASCA Consulting Group, Inc. 2008a; Babuska and Suri 1992; Chilton and Suri 1997). Therefore, contact stiffness is arbitrarily reduced, but not so much as the structure global stiffness is altered. That is why no exact suggestion for the contact stiffness is provided yet, and it is always assumed as an arbitrary parameter, which is usually estimated by empirical formula (Zhai et al. 2004; Pinho et al. 2006; Elmarakbi et al. 2009).

We make use of the concept of fracture cohesive zone to establish a physical interpretation for contact stiffness. The fracture cohesive zone theory suggests that fracturing process must be regarded as combination of material detachment and the cohesive zone, i.e., the damaged area surrounding the crack-tip. Since the model assumes no damage or stiffness reduction for particles, contact stiffness must represent the stiffness of the damaged material within the cohesive zone. Thus, before fracture initiation, the contact (initial) stiffness coefficient in tension and shear is suggested as follows:

$$k_{\mathrm{t}} = \frac{E}{w} \text{ and } k_{\mathrm{s}} = \frac{G}{w} \tag{11}$$

where E and G are the Young's and shear modulus of the undamaged material, and w is the thickness of the cohesive zone, perpendicular to the orientation of crack propagation.

Contact should gradually lose its stiffness upon opening or sliding in order to represent the cohesive zone damage. That is why the nonlinear (exponential) curves are adopted for the contact hardening behavior (Fig. 3). At the origin, the derivative of the curves equals the suggestions provided by Eq. 11. The slope of the curves then gradually decays as the contact displacement increases, and ultimately becomes zero.

The usual assumption of huge contact stiffness leads to a trivial thickness for the modeled cohesive zone. Therefore, this assumption is not only needed but also incorrect.

Two closed-form expressions are provided in Appendix for the cohesive zone thickness. Assuming them, the contact initial stiffness coefficients in plane-stress are related to material properties as follows:

$$k_{\mathrm{t}} = 3\beta \frac{E^2 \sigma_{\mathrm{t}}}{K_{\mathrm{IC}}^2} \text{ and } k_{\mathrm{s}} = 3\beta \frac{GE\sigma_{\mathrm{t}}}{K_{\mathrm{IIC}}^2} \tag{12}$$

and for plane-strain,

$$k_{\mathrm{t}} = 3\beta \frac{E^2 \sigma_{\mathrm{t}}}{(1-v^2)K_{\mathrm{IC}}^2} \text{ and } k_{\mathrm{s}} = 3\beta \frac{GE\sigma_{\mathrm{t}}}{(1-v^2)K_{\mathrm{IIC}}^2} \tag{13}$$

where β is a constant multiplier. The rest of the parameters are defined in Table 1.

The ratio of the initial stiffness coefficients is therefore

$$\frac{k_{\mathrm{s}}}{k_{\mathrm{t}}} = \frac{1}{2(1+v)} \left(\frac{K_{\mathrm{IC}}}{K_{\mathrm{IIC}}} \right)^2. \tag{14}$$

2.2.2 Particle Elastic Properties

Particle stiffness and that of contact together determine the model global stiffness. If contact stiffness is much higher than that of particle, its effect can be neglected. As a measure of particle deformability, E/d_{p} can be compared with the contact stiffness coefficients to examine the validity of this condition, where d_{p} denotes the particle edge size. As presented in Sect. 3.1.2, k_{t}, obtained from Eq. 12, is 2.61×10^3 MPa/mm whilst $E/d_{\mathrm{p}} = 6.50 \times 10^2$ MPa/mm.

Since the contact stiffness is one order greater than the particle deformability ratio, contacts do not have considerable effect on the model global elasticity. Therefore, the Young's modulus and the Poisson's ratio of the particles are assumed equal to those of the material.

$$E_{\mathrm{p}} = E \text{ and } v_{\mathrm{p}} = v \tag{15}$$

3 Model Calibration to Reproduce Compressive and Tensile Data of Rock

Although the microparameters related to the model elasticity, i.e., E_{p}, v_{p}, k_{t}, and k_{s}, are explicitly calculated, the others, i.e., t_{c}, c_{c}, and ϕ_{c}, are still unknown (note that given G_{f} and k_{t}, δ_{ut} is related to t_{c} and calculated through Eq. 10). Therefore, a calibration process in which the model response is compared with that of physical material is required to obtain t_{c}, c_{c}, and ϕ_{c}. The calibrated microparameters should be unique and result in the best quantitative and qualitative agreement between the model response and that of tested rock in terms of the Brazilian tensile strength (σ_{t}), uniaxial compressive strength (σ_{c}), internal cohesion (C) and internal friction angel (ϕ). Note that these four parameters are dependent of each other. If having three of them for a typical material, the forth is predictable by the Mohr–Coulomb equations. Therefore, σ_{t}, C and ϕ are considered as the parameters characterizing the model macroscopic response.

Since the model failure is controlled by contacts, σ_{t}, C, and ϕ of modeled material are related to t_{c}, c_{c}, and ϕ_{c} of contact. If finding these relations in an explicit form, we will have three equations with the same number of unknowns (i.e., t_{c}, c_{c}, and ϕ_{c}) that lead to a unique solution. The calibration process estimates these equations by a statistical approach called Design Of Experiment (DOE). The DOE provides a limited number of suggestions for the microparameters to simulate the laboratory tests. Using the results obtained from these simulations, the DOE eventually offers the equations in polynomial form of desirable order.

3.1 Numerical Simulation of Experiments

The following section describes material properties, numerical loading process, discrete element mesh, and boundary condition adopted to calibrate the model by simulating laboratory experiments including the uniaxial/triaxial compression and the Brazilian tension.

3.1.1 Material Properties, Boundary Condition, and Geometry of Test Specimens

Plaster mortar was used to make the specimens in laboratory. The mortar is made of plaster and water mixed by weight ratio of 1:0.65. All the specimens are cured for 5 days inside a chamber with the temperature of 25°C and the relative humidity of 55%. Mechanical properties of the plaster are measured as listed in Table 2. The details can be found in (Chiang 1997).

The compressive specimen is cylindrical, 54 mm in diameter, and 130 mm high. The Brazilian one is a disk

Table 2 Mechanical properties of the plaster

Young's modulus, E	1.3 GPa	Internal cohesion, C	1.75 MPa
Poisson's ratio, v	0.2	Internal friction angle, ϕ	40°
Fracture toughness in mode-I, K_{IC}	0.9 MPa.m$^{0.5}$	Brazilian tensile strength, σ_t	1.6 MPa
Fracture toughness mode-II, K_{IIC}	1.1 MPa.m$^{0.5}$	Uniaxial compressive strength, σ_c	7.5 MPa
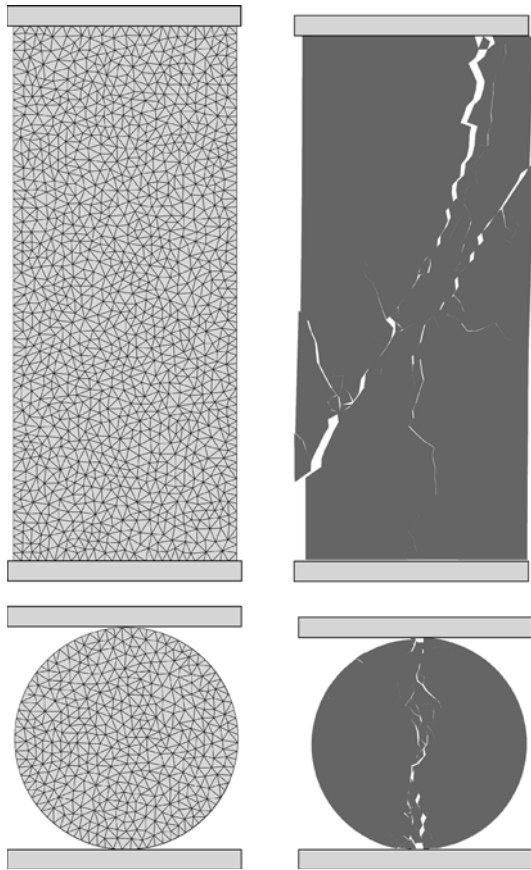
Fig. 5 Uniaxial compression and Brazilian tension models: geometry and boundary condition before failure (*left*), and predicted failure mode using calibrated microparameters (*right*)

with a diameter of 54 mm. They are placed between two steel platens whose interfacial friction is assumed negligible. The upper platen moves downward with a certain velocity, i.e., loading rate, while the lower one is fixed. The geometry and boundary condition of the samples are illustrated in Fig. 5.

3.1.2 Model Discretisation and Quasi-Static Analysis

The particle assemblage is generated arbitrarily to capture material heterogeneity and irregular fracture pattern. Both the samples consist of the triangular particles with an edge size of $d_p = 2.0 \pm 0.2$ mm. Each particle consists of one CST element.

According to the specimens' geometry, a plane-strain and a plane-stress analysis are adopted for the compressive and Brazilian models, respectively.

Using Eq. 15, Young's modules and Poisson's ratio for the particles are fixed at $E_p = 1.3$ GPa and $v_p = 0.2$. Given Eqs. 12 and 13, the tensile and shear initial stiffness coefficients of contact are obtained as $k_t = 2.61 \times 10^3$ MPa/mm and $k_s = 7.27 \times 10^2$ MPa/mm for the compressive sample, and $k_t = 2.50 \times 10^3$ MPa/mm and $k_s = 6.98 \times 10^2$ MPa/mm for the Brazilian one.

Since the solution algorithm of UDEC is dynamic, the rate of loading must be always defined. Assumedly, it should be the same as in practice, e.g., 0.02 mm/s, to simulate the actual test condition. Considering that the time step calculated by the code is about 10^{-7} s, one billion steps are needed to move the platen for 2 mm, i.e., the ultimate deformation of the plaster samples at compressive failure. This approach makes the analysis quite inefficient.

The only way feasible to restore the solution efficiency is raising the loading rate up to a reasonable level as well as applying sufficiently high numerical damping, e.g., 80% of the critical damping, to avoid any probable dynamic effect. The loading rate is therefore set to 10 mm/s for both the compression and tension tests.

Although the over damping removes the dynamic oscillations, it causes the stress wave to decelerate. Thus, a stress delay happens between two ends of the sample that annuls the needed quasi-static equilibrium for each solution step. To overcome this problem, we divide the loading process into *stages*. During each stage, the upper platen moves for 0.02 mm (i.e., 100th of the sample ultimate deformation). Then, it stops and the DEM analysis continues to reach static equilibrium. These stages repeat until the sample fails. During this process, reaction force at the lower support is continuously recorded to generate stress–strain curve and to estimate the sample strength.

3.2 Design of Experiment

Consisting of a group of statistical techniques, the DOE is an efficient discipline to quantitatively evaluate the relations between the measured responses of an experiment and the given input variables called factors (NIST/SEMATECH 2011; Sall 2007). The DOE begins with definition of experiment objectives and selection of input/output variables. In our purpose, the unknown microparameters and

the model macroscopic response are chosen as the factors and responses, respectively.

There are many different DOE methods, where the best choice depends on the number of factors involved and the level of accuracy required. Kennedy and Krouse (1999) presented the details for different DOE methods and categorized them based on experimental objectives they meet.

Depending on the experiment condition, a complete description of response behavior may need a linear, a quadratic or even a higher-order model. The probability of existing interaction between the microparameters makes us believe that a linear design does not satisfy our objective, and a quadratic model is strongly necessary.

3.2.1 Application of Central Composite Design

One of the DOEs used to predict the response quadratic curvature, is the Central Composite Design (CCD) [NIST/ SEMATECH 2011]. It suggests defining the factors at five coded levels, i.e., factorial (± 1), center (0), and star ($\pm \alpha$) points. Each pair of the factorial points represents the upper and lower bound expected for their corresponding factor. In three-dimensional space, they denote the eight vertices of a cube centered at the origin, with edges parallel to the Cartesian axes representing the coded factors (x_1, x_2 and x_3) and with an edge length of 2. The center points are then placed on the origin, and the star points are represented by the intersection of the axes and the circumscribed sphere of the cube. Therefore, $\alpha = 2^{3/4} \approx 1.682$. The levels 0, ± 1, $\pm \alpha$ and corresponding values for the microparameters are presented in Table 3.

The CCD offers a limited number of combinations of the factors at different coded levels. These combinations are collected in a matrix called coded design matrix as listed in Table 4. This matrix can be converted to the matrix of the real factors, i.e., microparameters, by the transformation formula expressed at the last column in Table 3. The laboratory tests are then simulated using each set of the CCD-suggested microparameters. These tests include the Brazilian tension, uniaxial, and triaxial compression tests on the samples shown in Fig. 5, where confining pressures, σ_3 applied in triaxial modeling, equals 0.5 and 1 MPa. Finally, the model macroscopic results, in terms of

tensile strength, internal cohesion, and internal friction angle are recorded as the DOE responses (Table 4), where internal cohesion and internal friction angle are calculated based on the obtained uniaxial and triaxial compressive strengths.

Note that the simulation is repeated for six times with the same microparameters but different particle arrangement (see 15th to 20th run in Table 4). This is because the particle assemblage is generated arbitrarily and two UDEC runs might produce slightly different results. Hence, the CCD predictively carries out this repetition to minimize the variability in modeling.

The targeted response parameters are statistically analyzed by applying the aforementioned data in the statistical software of JMP (Sall 2007). The individual parameters are evaluated using the Fischer test, and quadratic models of the form

$$X = \eta + \sum_i \lambda_i x_i + \sum_{i \neq j} \upsilon_{ij} x_i x_j + \sum_i \xi_i x_i^2 \quad (16)$$

are generated for each response parameter using multiple linear regression analysis and analysis of variance. X stands for the level of the measured response, i.e., σ_t, C and ϕ here. η is the intercept; λ_i, υ_{ij}, and ξ_i are the regression coefficients. x_i stands for the coded factors; $x_i x_j$ is the interaction between the main effects; and x_i^2 denotes the quadratic terms of the independent variables that are used to simulate the curvature of the designed surface.

Predictor equations containing only the significant terms are generated using a backward elimination procedure. A numerical optimization procedure using desirability approach is used to locate the optimal settings of the formulation variables in view to obtain the desired response (Park and Park 2010).

Using the data presented in Table 4, the following equations between the model macroscopic response and the coded factors are constructed:

$$\sigma_t = 0.75 + 0.28x_1 + 0.14x_2 + 0.03x_3 + 0.11x_1 x_2 \\ + 0.07x_1 x_3 - 0.03x_1 x_3 - 0.05x_1^2 - 0.12x_2^2 - 0.002x_3^2 \quad (17)$$

$$C = 1.80 + 0.48x_1 + 0.09x_2 + 0.15x_3 - 0.15x_1 x_2 \\ - 0.10x_1 x_3 + 0.11x_2 x_3 + 0.04x_1^2 - 0.37x_2^2 - 0.12x_3^2 \quad (18)$$

Table 3 Definition of factors and numerical value of microparameters at coded levels

Factor	Corresponding microparameter	Value of microparameter at coded levels					Transformation formula
		$-\alpha$	-1	0	$+1$	$+\alpha$	
x_1	Contact tensile strength, t_c	0.76	2.4	4.80	7.20	8.84	$t_c = 2.40 \times$ [coded level] $+ 4.80$
x_2	Contact cohesion, c_c	0.60	1.88	3.75	5.63	6.90	$c_c = 1.88 \times$ [coded level] $+ 3.75$
x_3	Contact friction angle, ϕ_c	29.91	34.00	40.00	46.00	50.09	$\phi_c = 6.00 \times$ [coded level] $+ 40.0$

Table 4 CCD-suggested design matrix and model obtained results

Run	Coded design matrix suggested by CCD			Microparameters matrix			Model predictions by using suggested microparameters		
	X_1	X_2	X_3	t_c	c_c	ϕ_c	σ_t	C	ϕ
1	−1	−1	−1	2.5	10.0	10.0	0.38	0.69	49.58
2	+1	−1	−1	7.5	10.0	10.0	0.47	1.91	21.78
3	−1	+1	−1	2.5	30.0	10.0	0.38	0.60	69.79
4	+1	+1	−1	7.5	30.0	10.0	1.04	1.86	62.67
5	−1	−1	+1	2.5	10.0	30.0	0.31	0.60	62.89
6	+1	−1	+1	7.5	10.0	30.0	0.81	2.09	39.91
7	−1	+1	+1	2.5	30.0	30.0	0.31	1.59	70.77
8	+1	+1	+1	7.5	30.0	30.0	1.11	1.81	70.57
9	−1.682	0	0	0.8	20.0	20.0	0.07	1.15	61.35
10	+1.682	0	0	9.2	20.0	20.0	1.14	2.55	50.97
11	0	−1.682	0	5.0	3.2	20.0	0.10	0.49	33.06
12	0	+1.682	0	5.0	36.8	20.0	0.70	0.87	73.53
13	0	0	−1.682	5.0	20.0	3.2	0.70	1.10	56.53
14	0	0	+1.682	5.0	20.0	36.8	0.76	1.68	66.39
15	0	0	0	5.0	20.0	20.0	0.70	1.71	57.46
16	0	0	0	5.0	20.0	20.0	0.63	1.77	60.41
17	0	0	0	5.0	20.0	20.0	0.80	1.93	56.67
18	0	0	0	5.0	20.0	20.0	0.90	2.14	53.39
19	0	0	0	5.0	20.0	20.0	0.71	1.53	60.82
20	0	0	0	5.0	20.0	20.0	0.79	1.71	57.67

$$\phi = 57.77 - 5.53x_1 + 12.28x_2 + 4.17x_3 + 5.43x_1x_2 + 1.47x_1x_3 - 2.82x_2x_3 - 0.75x_1^2 - 1.77x_2^2 + 1.12x_3^2. \tag{19}$$

Equations 17–19 form a quadratic system of simultaneous equations for the coded factors. Solving it for $\sigma_t = 1.6$ MPa, $C = 1.75$ MPa and $\phi = 40°$ of the plaster, $x_1 = 0.871$, $x_2 = 0.675$, and $x_3 = -0.583$. Using the transformation equations, the uncoded factors (target microparameters) are $t_c = 6.89$ MPa, $c_c = 5.02$ MPa, and $\phi_c = 36.50°$.

3.2.2 Verification of Calibrated Microparameters

All the microparameters, calculated for simulation of the plaster, are listed in Table 5.

Using these data, the tensile and compressive simulations are again repeated for five times. The results in terms of mean, standard deviation and relative error are listed in Table 6, where they show perfect agreements with the experimental measurements.

Figure 5 plots the model predictions for the failure mode of the tensile and compressive samples. As seen, the simulation predicts that the compressive sample breaks in an oblique shear surface. This is in agreement with the experimental observations, e.g., Paterson (1978) indicated the shear faulting as the characteristic failure process observed in soft rocks and plaster. The Brazilian sample also demonstrates typical splitting observed in laboratory.

3.3 Discussion

Comparing the multipliers in Eq. 17–19, the necessity of a quadratic DOE is justified. Equation 17 shows that the model tensile strength is more dependent on the contact tensile strength than its cohesion, where it is not much affected by the contact friction angle.

Table 5 List of target microparameters for simulation of plaster

E_p (GPa)	v_p	Compression (GPa/mm)		Tension (GPa/mm)		t_c (MPa)	c_c (MPa)	ϕ_c (°)
		k_t	k_s	k_t	k_s			
1.30	0.20	2.61	0.727	2.50	0.698	6.89	5.02	36.50

Table 6 Experimental properties of plaster versus model predictions

Property	E (GPa)	v	σ_t (MPa)	σ_c (MPa)	C (MPa)	ϕ (°)
Experimental value	1.3	0.20	1.6	7.5	1.75	40.0
Numerical mean	1.3	0.20	1.6	7.4	1.77	40.3
Standard deviation	0.01	0.01	0.04	0.16	0.04	0.59
Relative error (%)	1.54	4.03	3.13	4.01	3.43	2.51

The first- and second-order variables in Eq. 18 show that the model cohesion is more significantly related to the contact tensile strength than its cohesion and friction angle. Equation 19 presents that the contact tensile strength has an important role on the model friction angle, although the most significant effect comes from the contact cohesion.

These results indicate that contact tensile strength is the critical microparameter, which dominates the global failure of the simulation. This agrees with the experimental observations by Hazzard and Young (2000) mentioning that failure in rocks starts with creation of inter-mineral tensile fractures in parallel with the applied load. The coalescence of these microfractures creates a major failure surface as observed in laboratory and in the numerical modeling as well.

4 Reproduction of Shear Response of Rock Joint Samples

Using the microparameters calculated based on the compression and tension tests data, the shear behavior of joint specimens made of the same plaster is examined. The experimental results have been separately published, and their details can be found in (Chiang 1997; Yang and Chiang 2000).

4.1 Specimen Geometry and Boundary Condition

The joint samples include the simple joints having one single saw-tooth with an inclination of 30° and the composite joints consisting of two teeth at 15° and 30°. In all the samples, tooth height is fixed at 5.0 mm.

Figure 6 offers a schematic view of the joint samples together with the assigned boundary condition. The joint lower half is free to displace horizontally while vertically restrained. Conversely, the upper part is quite bonded by a rigid body prevented from any movement in the lateral direction. The rigid body is to obstruct the upper half from any global rotation. Consequently, dilation is allowed while rotation is not.

As experimentally observed (Yang and Chiang 2000), the material damage zone is limited to the joint tooth. Hence, only the teeth are permitted to break and the other parts of the specimen are assumed to behave elastically. The damage zone, i.e., joint tooth, is discretized by

particles with the average edge size of 0.2 mm. Figure 7 illustrates the particle assemblage forming a 30° asperity. A total of 393 and 1241 particles have been taken part in the model A and AB, respectively.

The simulation proceeds by first compressing the joints to reach the prescribed normal stress. Assuming plane-strain condition, the joints are then sheared by a controlled lateral displacement horizontally exerted to the lower half. To limit the computation time, a rate of 2 mm/s has been adopted.

4.2 Predictions and Discussion

Using the calibrated microparameters, the joints mechanical response is examined under normal stress of 0.39 and 1.47 MPa. A Coulomb friction law is assigned to the joint surface illustrated by a thick black line in Fig. 7. The penalty parameter to control the surface interpenetration is assumed to be equal to the contact tensile stiffness in plane-strain. This value is large enough to avoid any excessive overlap between the upper and lower parts of the specimens. The shear stiffness coefficient for the joint surface is fixed at 10 MPa/mm to best fit the elastic deformation of the joint in the pre-failure region. The friction angle of the joint surface is 35° (Chiang 1997).

4.2.1 Single-Tooth Joint

As shown in Fig. 8, the overall trend of the experimental response of the discontinuity, in terms of the joint strength and dilatancy, is satisfactorily reproduced, and the maximum and tail values of the shear stress are properly predicted.

Every time that one or several contacts fail, a sudden drop in the numerical response happens. However, the initial normal stress compresses the particles at broken contacts, and therefore the joint shear stress evolves again. These sequences of the drop and evolution give an oscillating appearance to the model shear response. Figure 9 demonstrates that the numerical and experimental failure patterns eventually are fairly similar.

4.2.2 Double-Tooth Joint

Both the high and low values of the normal pressure are applied on the composite joint. Although the peak shear

Fig. 6 Schematic representation of joint samples and applied boundary condition
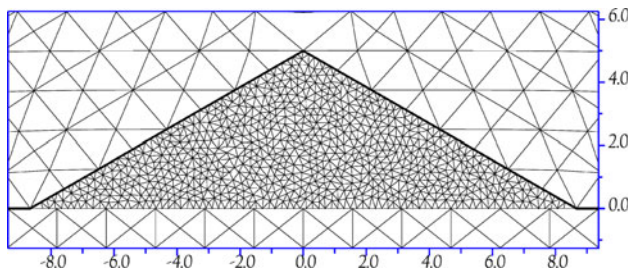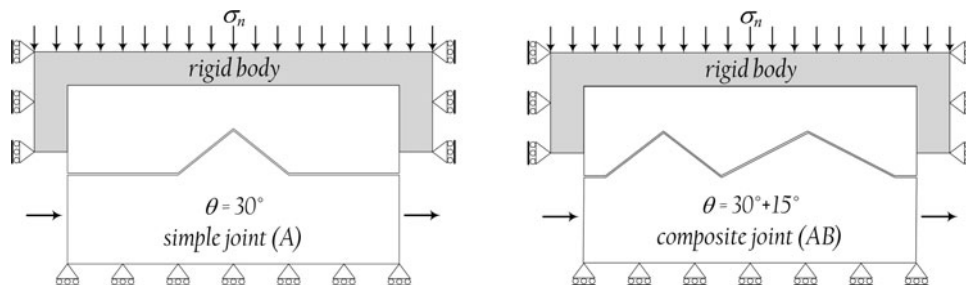

Fig. 7 Particle assemblage in a 30° joint asperity (units in millimeter)

strength is fairly reproduced under 1.47 MPa, there is a qualitative difference between the laboratory results and the numerical response in the post-failure stage (see Fig. 10). Comparing the test measurement, the model does not reproduce the flat zone and shows a larger drop in the shear stress, after which stress increases again. This is typical of a staggered contribution to the shear strength, i.e., the 30° tooth breaks and subsequently the 15° one are mobilized. This phenomenon causes a sudden fall in the numerical response. On the contrary, the smooth inclination in the experimental observation suggests that both the teeth are somehow sheared simultaneously. The reason of this difference might be a matter of the experimental boundary condition which is uncertain, or the 2D state of the numerical simulation versus the 3D nature of the experiment. Note that the numerical instabilities (mainly the excessive particles interpenetration) caused the

calculation to stop after 5 mm of shearing. To overcome this problem, we have to reduce the time step further, which makes the solution inefficient.

As seen in Fig. 10, the laboratory measurements are better predicted under 0.39 than 1.47 MPa, where both the peak and the residual shear strength are properly reproduced.

5 Conclusion

Using the discrete element code of UDEC, the compressive, tensile, and shear behaviors of rock was studied. The proposed numerical model considers the material as an assemblage of elastic particles interacting at their cohesive boundaries. These boundaries are viewed as flexible contact points. To introduce rock anisotropy, UDEC's contact model was developed to follow an orthotropic cohesive behavior, i.e., tensile and shear behavior of cohesive contacts are assumed different from each other.

As a part of research novelty, the model global responses, which represent the material macroscopic properties, were expressed in terms of the model microparameters. This was done by establishing original closed-form expressions and the application of statistical methods. The results of this part led to an ordered calibration process, which provided a unique set of the microparameters by which the model reproduced the standard compressive and tensile test data of rock. This was achieved while no

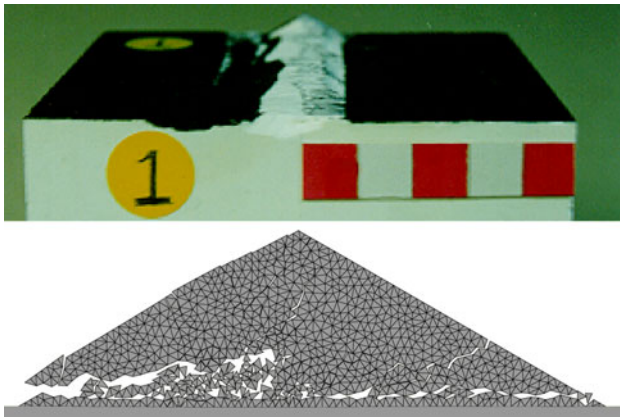**Fig. 8** Shear stress and dilation versus shear displacement for simple joint
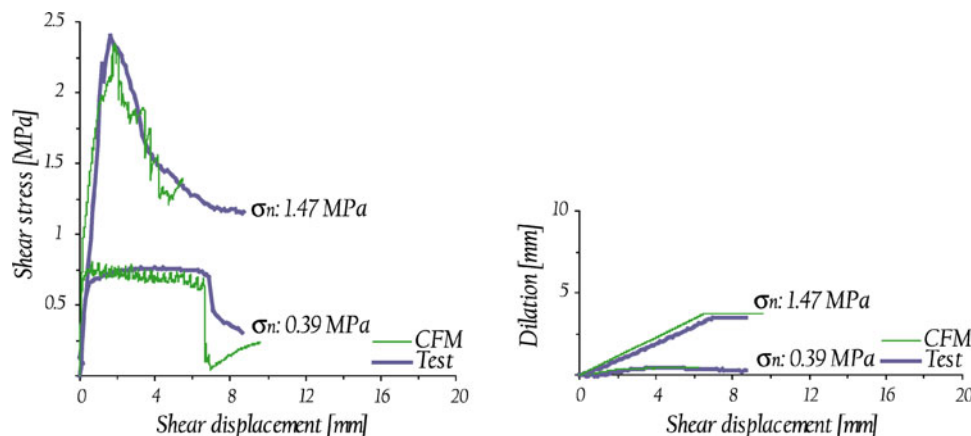
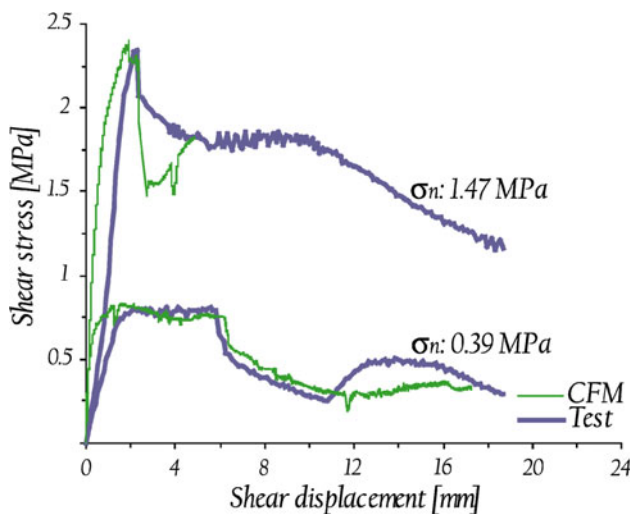**Fig. 9** Numerical failure mode versus laboratory observation for simple joint under 1.47 MPa

Fig. 10 Shear stress versus shear displacement for composite joint

extra effort, e.g., applying clump or cluster logic, was required.

The microparameters were calibrated for a tested plaster. Then, the joints, made of this plaster, were modeled. The results for the simple joint were excellent. The joint shear strength, dilation and failure mode were properly predicted. The model fitted the pre-failure response and the peak strength for the composite joint as well. However, there was a qualitative difference between the experiment and the numerical reproduction for high value of the joint normal pressure, where the model showed a significant drop in the shear stress following the peak shear strength. Nevertheless, the model succeeded to match the laboratory results of the composite joint under low normal pressure.

The model reproduced the actual material fracture and fragmentation while no plasticity, flow rule, or damage law was required. These results encourage us in future applications of the DEM for simulating material failure and fracture process.

Appendix: Estimation of Cohesive Zone Thickness

This section provides an estimation for the cohesive zone thickness in terms of the material mechanical properties.

Material Strength in Molecular Mechanics

A material cracks when the sufficient stress and energy are applied to break the inter-molecular bonds. These bonds hold the molecules together and their strength is supplied by the attractive forces between the molecules. Many equations have been proposed to formulate this force and its potential energy. The Lennard-Jones potential is a simple and extensively used function in this way (Griebel 2007),

$$\Psi(x) = \alpha\varepsilon\left[\left(\frac{\xi}{x}\right)^n - \left(\frac{\xi}{x}\right)^m\right] \tag{20}$$

where $m < n$. x denotes the separation distance between two adjacent molecules, and

$$\alpha = \frac{1}{n-m}\left(\frac{n^n}{m^m}\right)^{\frac{1}{n-m}}. \tag{21}$$

This potential is parameterized by ξ and ε. As depicted in Fig. 11, ε describes the depth of the potential and thereby the strength of the repulsive and attractive forces. The value ξ parameterizes the zero crossing of the potential. The integer m and n are dependent of the material molecular nature and are more commonly among 6–16.

As the potential derivative with respect to x, the inter-molecular force $P(x)$ is written as

$$P(x) = \frac{\partial\Psi}{\partial x} = \frac{\alpha\varepsilon}{x}\left[-n\left(\frac{\xi}{x}\right)^n + m\left(\frac{\xi}{x}\right)^m\right]. \tag{22}$$
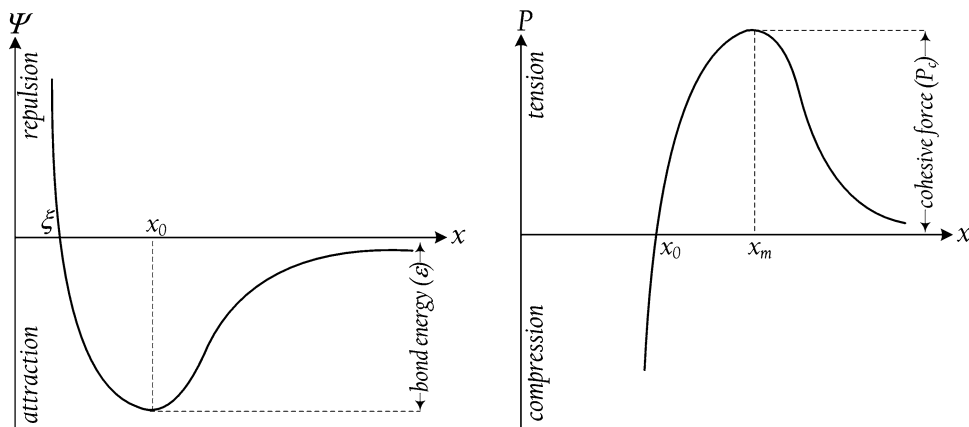
The peak value of the intermolecular force, which is called cohesive force, P_c, happens at x_m as shown in Fig. 11. Solving the derivative of $P(x)$ for x,

$$x_m = \xi\left(\frac{n(n+1)}{m(m+1)}\right)^{\frac{1}{n-m}} \tag{23}$$

Substituting x_m into Eq. 22 leads to

$$P_c = \alpha\frac{\varepsilon}{\xi}\left(-n\left(\frac{n(n+1)}{m(m+1)}\right)^{\frac{-n-1}{n-m}} + m\left(\frac{n(n+1)}{m(m+1)}\right)^{\frac{-m-1}{n-m}}\right). \tag{24}$$

Fig. 11 Plots of Lennard-Jones' potential function (*left*) and intermolecular force (*right*)

The equilibrium spacing between two molecules, x_o occurs when the potential energy is at a minimum or the force is zero (see Fig. 11). Thus, if solving Eq. 22 for x,

$$x_0 = \xi\left(\frac{n}{m}\right)^{\frac{1}{n-m}}. \tag{25}$$

In unit volume of a perfect material, there should ideally exist $1/x_0^3$ molecules and $3/x_0^3$ bonds. However, the number of molecules and bonds in reality never reaches these predictions because of material imperfections such as molecular vacancies and voids. Therefore, the number of existing bonds, n_b, can be defined as

$$n_b = \gamma\frac{3}{x_0^3} \tag{26}$$

where γ is a multiplier, smaller than one, that indicates the rate of the existing bonds per unit volume of the physical material.

For perfect material, P_c/x_0^2 estimates the material tensile strength, σ_t. However, σ_t never reaches P_c/x_0^2 again due to material imperfections. Given the definition of γ, σ_t can be estimated as

$$\sigma_t = \gamma\frac{P_c}{x_0^2}. \tag{27}$$

Material Fracturing

A tensile force is required to increase the separation distance from the equilibrium value. If this force exceeds the cohesive force the bond is completely severed, and the material starts cracking. The energy needed to break a single bond, called bond energy, is calculated as follows:

$$U = \int_{x_0}^{\infty} P(x)\mathrm{d}x = \Psi(x)\big]_{x_0}^{\infty} = -\Psi(x_0) = \varepsilon. \tag{28}$$

After material cracked, a high-stress concentration will be created at the areas close to the crack-tip. Therefore, bond rupture takes place across an extended crack tip, i.e., fracture process zone. As Fig. 12 suggests, the number of bonds located at the cohesive zone, n_{bc} can be estimated by the multiplication of n_b by the volume of the cohesive zone:

$$n_{bc} = 3\gamma\frac{wa_z}{x_0^3} \tag{29}$$

where w and a_z denotes the thickness and the surface of the cohesive zone, respectively.

When a bond breaks, a quantity of energy equal to U is dissipated. The accumulation of these energies over the cohesive zone surface supplies the energy dissipation through fracturing. Therefore, the Griffith's fracture energy G_f, defined as the rate of total energy release per unit cracked area, is expressed as

$$G_f = \frac{n_{bc}\varepsilon}{a_z} = 3\gamma\frac{w\varepsilon}{x_0^3}. \tag{30}$$

Substituting the parameter ε obtained from Eq. 24 into the above relation,

Fig. 12 Fracture representation in simulation (*left*) and in molecular-scale (*right*)

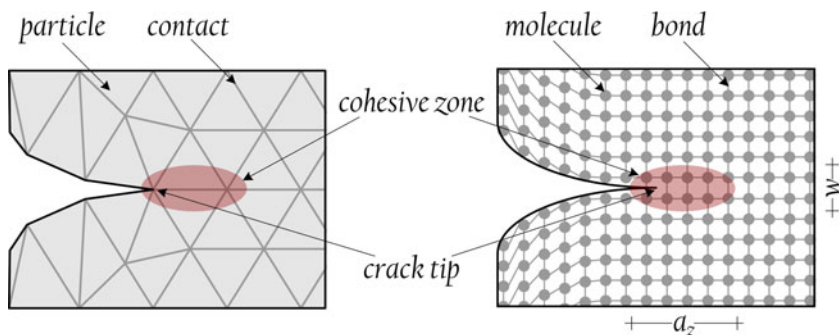**Table 7** Values of β for common values of m and n

m	$n = 13$	$n = 14$	$n = 15$	$n = 16$	$n = 17$	$n = 18$
8	0.30	0.29	0.28	0.27	0.26	0.26
9	0.28	0.27	0.26	0.25	0.25	0.24
10	0.26	0.25	0.24	0.24	0.23	0.22
11	0.25	0.24	0.23	0.22	0.22	0.21
12	0.24	0.23	0.22	0.21	0.21	0.20

$$G_f = 3\frac{\gamma w \xi}{\alpha x_0^3} P_c \left(-n \left(\frac{n(n+1)}{m(m+1)} \right)^{\frac{-n-1}{n-m}} + m \left(\frac{n(n+1)}{m(m+1)} \right)^{\frac{-m-1}{n-m}} \right)^{-1} \tag{31}$$

Substituting P_c by Eq. 27 and x_0 by Eq. 25 into Eq. 31, and solving it for w, the cohesive zone thickness is estimated in terms of σ_t and G_f as follows:

$$w = \frac{1}{3\beta} \frac{G_f}{\sigma_t} \tag{32}$$

where

$$\beta = \frac{\frac{1}{m} - \frac{1}{n}}{\left(\frac{m+1}{n+1} \right)^{\frac{m+1}{n-m}} - \left(\frac{m+1}{n+1} \right)^{\frac{n+1}{n-m}}} \tag{33}$$

depends on the integers m and n. Table 7 shows that β is relatively constant at 0.25 for common values of $m \in [8, 12]$ and $n \in [13, 18]$.

In mixed mode fracturing, G_f is stated as

$$G_f = \frac{K_{IC}^2}{\tilde{E}} + \frac{K_{IIC}^2}{\tilde{E}} \tag{34}$$

where $\tilde{E} = E$ for plain-stress, and $\tilde{E} = E/(1 - v^2)$ for plain-strain. If contact undergoes pure tension,

$$w = \frac{1}{3\beta \tilde{E} \sigma_t} K_{IC}^2 \tag{35}$$

and in case of pure sliding

$$w = \frac{1}{3\beta \tilde{E} \sigma_t} K_{IIC}^2 \tag{36}$$

References

Babuska I, Suri M (1992) On locking and robustness in the finite-element method. SIAM J Numer Anal 29(5):1261–1293
Chiang DY (1997) Experimental study on the degradation of shear behavior of tooth-shaped joints. Master thesis of Civil Engineering, Tamkang University, Taipei, Taiwan
Chilton L, Suri M (1997) On the selection of a locking-free hp element for elasticity problems. Int J Numer Methods Eng 40(11):2045–2062
Cho N, Martin CD et al (2007) A clumped particle model for rock. Int J Rock Mech Mining Sci 44(7):997–1010
Cundall PA (1971) A computer model for simulating progressive, large scale movements in blocky rock systems. In: Proceedings of the international symposium on rock fracture. Nancy
Diederich MS (2000) Instability of hard rock masses: the role of tensile damage and relaxation. PhD thesis, University of Waterloo
Elmarakbi AM, Hu N et al (2009) Finite element simulation of delamination growth in composite materials using LS-DYNA. Compos Sci Technol 69(14):2383–2391
Griebel M, Knapek S et al (2007) Numerical simulation in molecular dynamics: numerics, algorithms, parallelization, applications. Springer, Berlin
Hazzard JF, Young RP (2000) Micromechanical modelling of cracking and failure in brittle rocks. J Geophys Res 105:16683–16697
Hoek E, Brown ET (1998) Practical estimates of rock mass strength. Int J Rock Mech Mining Sci 34:1165–1186
ITASCA Consulting Group, Inc. (2008a) PFC2D and PFC3D manuals
ITASCA Consulting Group, Inc. (2008b) UDEC and 3DEC manual
Jing L, Stephansson O (2007) Fundamentals of discrete element methods for rock engineering. In: Theory and application. Elsevier, Amsterdam
Kazerani T, Zhao J (2010) Micromechanical parameters in bonded particle method for modeling of brittle material failure. Int J Numer Anal Methods Geomech 34(18):1877–1895. doi: 10.1002/nag.884
Kennedy M, Krouse D (1999) Strategies for improving fermentation medium performance: a review. J Ind Microbiol Biotechnol 23(6):456–475
Lobo-Guerrero S, Vallejo LE (2010) Fibre-reinforcement of granular materials: DEM visualisation and analysis. Geomech Geoeng 5(2):79–89
Lobo-Guerrero S, Vallejo LE et al (2006) Visualization of crushing evolution in granular materials under compression using DEM. Int J Geomech 6(3):195–200
Mahabadi OK, Grasselli G et al (2010) Y-GUI: a graphical user interface and pre-processor for the combined finite–discrete element code, Y2D, incorporating material heterogeneity. Comput Geosci 36(2):241–252
Park HJ, Park SH (2010) Extension of central composite design for second-order response surface model building. Commun Stat Theory Methods 39(7):1202–1211
Paterson MS (1978) Experimental rock deformation, the brittle field. Springer, Berlin
Pinho ST, Iannucci L et al (2006) Formulation and implementation of decohesion elements in an explicit finite element code. Composites A Appl Sci Manuf 37(5):778–789
Potyondy DO, Cundall PA (2004) A bonded-particle model for rock. Int J Rock Mech Mining Sci 41(8):1329–1364
Sall J, Creighton L et al (2007) JMP Start Statistics: a guide to statistics and data analysis using JMP, 4th edn. SAS Press
Schöpfer MPJ, Abe S et al (2009) The impact of porosity and crack density on the elasticity, strength and friction of cohesive granular materials: insights from DEM modelling. Int J Rock Mech Mining Sci 46(2):250–261
Wang Y, Tonon F (2009) Modeling Lac du Bonnet granite using a discrete element model. Int J Rock Mech Mining Sci 46(7):1124–1135
Xu XP, Needleman A (1996) Numerical simulations of dynamic crack growth along an interface. Int J Fract 74(4):289–324
NIST/SEMATECH e-handbook of statistical methods (2011). http://www.itl.nist.gov/div898/handbook. Accessed 16 Feb 2011
Yang ZY, Chiang DY (2000) An experimental study on the progressive shear behavior of rock joints with tooth-shaped asperities. Int J Rock Mech Mining Sci 37(8):1247–1259

Yoon J (2007) Application of experimental design and optimization to PFC model calibration in uniaxial compression simulation. Int J Rock Mech Mining Sci 44(6):871–889

Zhai J, Tomar V et al (2004) Micromechanical simulation of dynamic fracture using the cohesive finite element method. J Eng Mater Technol 126(2):179–191